Published in final edited form as:
Sci Transl Med. 2010 March 24; 2(24): 24ra22. doi:10.1126/scitranslmed.3000738.

A Conformal, Bio-interfaced Class of Silicon Electronics for Mapping Cardiac Electrophysiology

Jonathan Viventi[1,⊥], **Dae-Hyeong Kim**[2,⊥], **Joshua D. Moss**[3], **Yun-Soung Kim**[2], **Justin A. Blanco**[1], **Nicholas Annetta**[4], **Andrew Hicks**[1], **Jianliang Xiao**[5], **Younggang Huang**[5], **David J. Callans**[3], **John A. Rogers**[2,*], and **Brian Litt**[1,6,*]

[1] Department of Bioengineering, University of Pennsylvania, Philadelphia, PA 19104 USA

[2] Department of Materials Science and Engineering, Beckman Institute for Advanced Science and Technology, and Frederick Seitz Materials Research Laboratory, University of Illinois at Urbana-Champaign, Urbana, Illinois 61801 USA

[3] Department of Cardiology, Hospital of the University of Pennsylvania, 9 Founders Pavilion, 3400 Spruce Street, Philadelphia, PA 19104 USA

[4] Department of Electrical and Systems Engineering, University of Pennsylvania, Philadelphia, PA 19104 USA

[5] Department of Mechanical Engineering and Department of Civil and Environmental Engineering, Northwestern University, Evanston, IL 60208

[6] Penn Epilepsy Center, Department of Neurology, Hospital of the University of Pennsylvania, 3 West Gates, 3400 Spruce Street, Philadelphia, PA 19104 USA

Abstract

The sophistication and resolution of current implantable medical devices are limited by the need connect each sensor separately to data acquisition systems. The ability of these devices to sample and modulate tissues is further limited by the rigid, planar nature of the electronics and the electrode-tissue interface. Here, we report the development of a class of mechanically flexible silicon electronics for measuring signals in an intimate, conformal integrated mode on the dynamic, three dimensional surfaces of soft tissues in the human body. We illustrate this technology in sensor systems composed of 2016 silicon nanomembrane transistors configured to record electrical activity directly from the curved, wet surface of a beating heart in vivo. The devices sample with simultaneous sub-millimeter and sub-millisecond resolution through 288 amplified and multiplexed channels. We use these systems to map the spread of spontaneous and paced ventricular depolarization in real time, at high resolution, on the epicardial surface in a porcine animal model. This clinical-scale demonstration represents one example of many possible uses of this technology in minimally invasive medical devices.

[Conformal electronics and sensors intimately integrated with living tissues enable a new generation of implantable devices capable of addressing important problems in human health.]

* To whom correspondence should be addressed. littb@mail.med.upenn.edu; jrogers@uiuc.edu .
⊥J. Viventi and D.-H. Kim contributed equally.

Author Contributions: J.V., D.H.K., J.D.M., Y.S.K., N.A., D.J.C., J.X, Y.H., J.A.R. and B.L. designed the experiments. J.V., D.H.K., J.D.M., Y.S.K., D.J.C., J.X and Y.H. performed experiments and analysis. J.V., D.H.K., J.D.M., D.J.C., J.A.B., J.A.R. and B.L wrote the paper.

INTRODUCTION

Conventional tools for managing and treating cardiac arrhythmias use sparse arrays of rigid electrodes that probe potentials at the surface of cardiac tissue at one or a few spatial locations at a time. During mapping, these sensors are moved from place to place to record from discrete sites on the heart. Sequential local recordings are then "stitched" together with software to render a complete representation of cardiac electrical activity over a region of interest. The iterative nature of this approach prolongs electrophysiology (EP) procedures and prevents real time mapping of transient abnormal rhythms (12,13). One conceivable means to address this problem is to integrate distributed sensors and electronics over the surface of the heart to provide full, spatio-temporal evaluation of EP in real time. At present, however, all forms of high-performance electronics are built on the hard, rigid and brittle surfaces of semiconductor wafers, in formats that are inherently incompatible with establishing intimate, large area interfaces with the body. Newer flexible, stretchable electronics have the potential to avoid these limitations, but existing devices do not offer the levels of integration or performance needed to be clinically useful (1-11). In addition, these technologies cannot yet operate when immersed in biological fluids, as required for any realistic medical use (1-9).

Here we report advances that overcome these challenges, to enable high performance, conformal electronic systems capable of intimate integration with dynamic, living biological tissues. We apply this approach in a sensor system configured to measure cardiac electrophysiological activity with high temporal and spatial resolution and we validate its performance in live animal tests in situ.

RESULTS

Fabrication

Figure 1 illustrates the fabrication sequence for a single unit, or "cell" (Fig. 1A-D), and for the completed device (Fig. 1E). Each cell consists of a contact pad that serves as an electrical interface to the tissue and an associated amplifier and multiplexer. The device includes an 18 by 16 array of such amplified electrodes to provide a total of 288 measurement points spaced 800 μm apart and covering a total area of 14.4 mm by 12.8 mm (Fig. 1). Each unit cell comprises 7 n-type metal–oxide–semiconductor (nMOS) field-effect transistors for a total of 2016. Integrated multiplexing circuitry, enables the use of only 36 wires to connect all 288 measurement points to external data acquisition and control units.

The transistors and interconnects were formed in four layers. In the first step, transfer printing delivers to a flexible plastic substrate (polyimide; ~25 μm thick) an organized collection of single crystalline, semiconductor grade silicon nanomembranes (260 nm) with patterned regions of n-type (phosphorus) doping (Fig. 1A). Plasma-enhanced chemical vapor deposition of SiO_2 (~100 nm) at reduced temperatures yields a gate dielectric through which source/drain contact openings are formed by photolithography and etching in buffered oxide etchant. Electron beam evaporation, photolithography and wet etching define the first layer of metal interconnect, including source, drain and gate contacts (Fig. 1B). Similarly fabricated second and third metal layers form the column and row addressing electrodes (Fig. 1C, D). A thin layer of spin cast polyimide (1.4 μm) with etched via holes provides the interlayer dielectric between the first and second metal layers; a trilayer organic/inorganic stack (polyimide/Si_3N_4/epoxy 1.4 μm/80 nm/9 μm) and a single layer of epoxy (9 μm) forms a similar interlayer for the second and third and third and fourth metal layers, respectively. Details are outlined in Figs. S1 to S5 of the SM.

Design

These different layers locate the circuit at the neutral mechanical plane and ensure reliable operation when immersed in saline solution, as described below. The top metal layer defines the surface electrodes (Au pads, 250×250 μm) that contact the cardiac tissue and connect to the underlying circuits through vertical interconnect access (VIA) holes. These electrodes have output impedances of 100 kOhm ± 10% at 1 kHz, as measured with a similarly designed passive electrode array immersed in normal saline (0.9%) solution. (Measuring the output impedance of the metal electrodes is not currently possible while they are integrated with the active circuitry.) The entire device connects to a data acquisition system through an anisotropic conductive film (ACF) connector with 36 contacts. See Fig. S6 for more details and for dimensions of devices.

The right panels of Fig. 1C and Fig. 2A provide annotated images and circuit diagrams, respectively, of the amplifier and the multiplexing transistor. The amplifier uses a source-follower configuration with current gain (Fig. S7). The multiplexing transistor enables readout of all inputs via programmed, sequential addressing of each row of electrodes, thereby providing a 16 times reduction in the required number of output wires compared to a non-multiplexed electrode array.

The schematic in Fig. 2B illustrates how the unit cell in Fig. 2A can be connected to other unit cells to create the multiplexed signal output. This basic layout allows the design to be easily scaled up to larger overall array sizes, while maintaining the spatial resolution of the array and without adding exponentially more wires. During multiplexed sampling, one row of electrodes at a time is selected by driving one of the row select signals, such as R_0 (highlighted in blue in Fig. 2B.), high and all of the others low (R_1 .. R_n, where R_1 is highlighted in green). This allows the unit cells in that row to drive the column output lines (C_0 … C_n, where C_0 is highlighted in red), which are connected to a high-speed analog to digital converter (Fig. S8). Row select signals are rapidly cycled to sample all electrodes on the array.

Properties

The multiplexing transistor exhibits an on/off ratio and electron mobility of ~10^5 and ~490 cm^2/Vs, respectively (Fig. 2C). The high mobility of single crystalline silicon, compared to organics or other materials for flexible electronics, enables the amplifier to have a high bandwidth (Fig. 2D), and the multiplexer to switch quickly (Fig. 2E), even for the relatively coarse dimensions of the devices reported here (channel lengths of ~40 μm). The switching time (about 5 μs) is limited, however, by the slew rate of the external row select signals provided to the array, as shown in blue and green in Fig. 2E. We also determined the percentage of the final voltage value attained during the allotted settling time, averaged across all of the electrodes, for increasing multiplexing frequency (Fig. 2F). Multiplexing rates up to 200 kHz were measured, yielding usable sampling rates up to 12.5 kHz per electrode. The signal to noise ratio (SNR) for the system remains constant up to 200 kHz multiplexing frequency (Fig. S9). The SNR calculation was signal to noise and distortion (SINAD) for a 50 mV peak to peak sine wave at 20 Hz. The high value for SINAD indicates that there was very little non-linear distortion introduced by the device. The SNR measurements (Fig. S9) and the voltage shifts between adjacent channels (Fig. 2E) indicate that crosstalk is negligible for typical signal levels.

As the slew rate of the row select signals is increased via improvements in the data acquisition system, the multiplexing rate can be further increased. In experiments described below, the 16 row select signals were cycled at 10 kHz, yielding a sampling rate of 625 Hz per active electrode, with all 16 electrodes in a given row thus sampled sequentially. The

multiplexed analog signals were synchronously sampled at 50 kHz, with 5× oversampling per switch interval to improve the SNR.

Mechanical Flexibility

We used analytical mechanics modeling to elucidate the bend-induced strains in all layers of the devices used in our animal experiments. For bend radii of ~5 cm, typical of those used in commercially available electrophysiology (EP) catheter designs, maximum strains in the Si and SiO_2 are found to be 0.001% and 0.0001%, respectively. These values are orders of magnitude below the fracture strain for Si and SiO_2 (~1%), and they are also significantly less than those expected to alter their electrical performance. The induced strains remain below the fracture limits to radii of curvature as small as 500 μm (Fig. S10), thereby enabling the array to be rolled into a catheter of only a few millimeters in diameter and unrolled once delivered to the target tissue. Tight folding tests, to radii as small as 500 μm, confirmed that the circuits remain operational under such conditions.

We also tested whether the bending stiffness of the circuit is sufficiently low to allow conformal wrapping on the moist surface of the cardiac tissue. These mechanics can be modeled by comparing the system energy for a circuit in a flat configuration to one in a wrapped state (Fig. S11). The result is that wrapping is energetically favored when $\gamma > B / 2R^2$, where γ is the adhesion energy between the circuit and the tissue, R is the radius of curvature, and B is the bending stiffness of the circuit. By using R~2.5 cm and a computed value of B, one finds that wrapping is the preferred configuration for cases where $\gamma > 34.7$ mJ/m^2. The reported value of adhesion energy between two wet surfaces is ~75-150 mJ/m^2 (14-16). Our model therefore predicts that the circuits will naturally wrap around the partially wet surface of the cardiac tissue without any separate mechanism to ensure adhesion. This result was validated in our experiments in the porcine model.

Operation in Biological Fluids

For use in clinical settings, the circuit must provide sustained operation while immersed in the body's fluids. We found that our inorganic/organic encapsulation of the circuit serves as an effective water barrier. We immersed the circuit in a saline bath to test for leakage currents from either power supply by creating a conduction path from the device to a separate ground electrode in the bath (Fig. 2G). We selected a cutoff value of 10 μA, consistent with the International Electrotechnical Commission standards for medical electronic equipment (IEC 60601-1). Approximately 75% of the fabricated devices (all electrodes included) passed the leakage current test. Randomly selected samples that passed the initial leakage current test were tested for long-term reliability in the saline bath and found to operate for greater than 3 hours while maintaining a leakage current less than 10 μA. Figure 2H shows the device response to a 10 Hz sine wave input before and after saline immersion for 3 hours, verifying that there were negligible changes in circuit properties. Results with a 5 Hz input are also displayed in Fig. S12.

Cardiac Monitoring in Pigs

In vivo experiments were performed in two normal 80 to 90 pound male Yorkshire pigs. The heart was surgically exposed via a median sternotomy and subsequent pericardiotomy. Flexible devices were then placed on the epicardial surface while under direct visualization (Fig. 3A, S13 and Movie M1). The device adhered to the curvilinear surface of the heart, even during the vigorous cardiac motion of rapid pacing. Fig. 3B shows motion snapshots at various stages of the cardiac cycle; the blue lines highlight the dynamic variations in the surface shape associated with maintaining conformal contact. Given the average heart rate of ~ 77 beats per minute (BPM) during *in vivo* experiments and a recording duration of ~ 137 minutes, the device provided reliable data over the course of >10,000 bending cycles.

Unipolar voltage data were recorded from all 288 electrodes with the sampling and multiplexing strategy described above. Baseline electrogram data were collected in sinus rhythm with the array in multiple positions and orientations on the epicardial surface. We also recorded while pacing the heart from multiple locations relative to the array. The distance of the pacing electrode from the array varied from 2 to 5 cm during different experiments. The pacing electrodes were 1.25 mm wide and spaced 2.5 mm apart (bipolar pacing). The pacing current was 10 mA with a pulse-width of 2 msec.

Figure 3C shows the array positioned over the left anterior descending (LAD) coronary artery (yellow arrow), with the pacing catheter (white arrow) positioned just inferior to the array. The presence of the epicardial coronary artery did not cause any noticeable distortion to the recording. As predicted previously, the adhesion energy between the wet surface and the electrode array was sufficient to hold the array onto the surface of the heart. If the pericardium were intact, as it would be during a catheter-based procedure, the electrode would be bathed in fluid and the forces would be quite different. In this case, we anticipate that tension of the space between the epicardium and the pericardium will hold the array in contact. The color coded map in Fig. 3C shows a visual representation of the data collected from the device, with the procedures described below.

Data from all channels were filtered and processed with custom MATLAB software to determine the relative activation time at each contact by comparing the time of the maximum negative slope (*dV/dt*) of the unipolar electrogram to the maximum negative slope of the average electrogram of all 288 channels. These activation times were then used to generate isochronal maps showing propagation of paced and unpaced cardiac depolarization wavefronts spreading across the array for a variety of recording sites and pacing conditions (Movie M2 and Fig. S24). Sample voltage trace data from a single channel without remote pacing are shown in Figure 4A. The noise level of the recording was very low (Fig. 4A, inset) with a SNR of approximately 34 dB. Voltage data for all channels taken at 4 points in time and plotted as a color image show a wave of cardiac activation moving from the left side of the array to the right side (Fig. 4B). Dashed lines plotted on an average voltage trace collected from all of the electrodes illustrate the instant in time that each frame in Fig. 4B was taken (Fig. 4C). A similar plot of externally paced data shows a wave of cardiac activation moving from the right side of the array to the left side (Fig. S16). Figure S24 and movie M2 detail all of the voltage data presented in Fig. 4B. The response of the electrodes was uniform, as we determined by plotting the average peak amplitude of the cardiac activation (Fig. S14).

We used the voltage data to develop an isochronal activation map, illustrating the natural activation pattern of the heart (Fig. S15A). Data from 3 of the 18 columns were removed due to failures in the metal interconnections, related to imperfections in the fabrication. Conduction velocities can be computed even with defective columns by linear interpolation using knowledge of the spatial locations of the remaining columns. All of the remaining channels and all rows functioned properly.

We also collected data with remote pacing and generated isochronal maps by pacing from three different locations relative to the array (Fig. 4E and S15B). A sample of the raw voltage data from a single channel is shown to illustrate the typical waveforms (Fig. 4D). The complete data used to generate the isochronal map in the left and right panels of Fig. 4E are provided in Figures S25 – S26 and movies M3 - M4 respectively.

On the basis of the relative activation times, conduction velocity across the array (transverse to fiber axis) was 0.9 mm/msec (Fig. 4E); the velocity in the longitudinal direction (approximately parallel to the orientation of the LAD) was faster by a factor of 3 (Fig.

S14B). These results are consistent with anisotropic conduction properties measured in previous studies using mammalian hearts (17,18).

Sample distance vs. activation plots for selected rows of the electrode array following the arrows in Fig. 4E further illustrate the linear wavefront propagation recorded by the device (Fig. 4F).

DISCUSSION

The conformal, bio-interfaced electronic systems described here represent a fundamentally different class of EP device that can automatically map entire regions of the epicardial surface at high speed without the need for manual movement or operation. High performance transistors in circuits with medium-scale levels of integration (~2000 transistors) and specialized designs on plastic substrates offer features that meet the challenging requirements for use in clinical cardiology: (1) local current amplification for accurate measurements of small electrical potentials (~mV) associated with cardiac conduction, (2) high speed operation (approaching ~MHz) to enable sampling of fast signals (~ms), (3) actively multiplexed addressing schemes for high density arrays of sensors (288 independent channels) with minimal numbers of external connections (36 wires), (4) water-proof designs for reliable operation when completely submerged in pericardial fluids for extended periods (hours), (5) ultra-low bending stiffness for robust adhesion to the beating, epicardial surface by physical lamination, without adhesives or penetrating pins and (6) neutral mechanical plane layouts to eliminate any variation in the system behavior with bending.

A number of improvements are possible that would enhance the device presented above. For clinical applications, platinum or platinum-iridium should be used instead of gold, because of lower impedance. Increasing channel yield in the device will require further optimization of processing conditions and might demand the use of cleanroom facilities configured for manufacturing, rather than academic research. Finally, although the system noise is acceptable for the cardiac application, it could be reduced further though the use of complementary circuits and analog to digital converters with improved resolution.

In addition to advances in performance, additional functionality can be considered. For example, with straightforward additions to the circuits and external control, the same systems could provide multi-site cardiac pacing with closed-loop feedback of local ventricular contractility or cardiac output measurements via distributed arrays of active sensory and stimulation electrodes. Furthermore, the mechanical properties of the circuits permit their packaging in catheter-based delivery systems, with the ability to deploy on and conform to large and small, irregular curvilinear surfaces in the body. Pursuing these possibilities represents a promising direction for future work.

More generally, the results presented here suggest a platform for clinically relevant implantable devices that overcome limitations associated with the long-standing requirement of one wire for each sensor through the use of active electronics formed on flexible sheets of plastic. The capacity to intimately integrate the full power of modern semiconductor technology with the soft, fluid-bathed, curvilinear and moving surfaces of the human body has major implications for human health, via advanced devices for diagnostic, therapeutic and surgical applications.

MATERIALS AND METHODS

Circuit Design

Each unit cell incorporates an nMOS based source-follower amplifier configuration. This circuit provides significant current gain to enable fast switching of the multiplexers by supplying the current needed to charge the parasitic output capacitances. These unintended additional capacitances come from several sources, including the inactive multiplexing transistors in a given column, the ~2 foot long cables that connect the electrode array to the interface circuit board, the circuit board itself and the input capacitance of its buffer amplifiers.

Power is supplied to the array via the +V and −V connections. Split power supplies are utilized to allow the physiologic signals biased around 0 V to remain well within the linear input range of the amplifiers. The linear input range is approximately (−V + Vt) to +V, where Vt is the transistor threshold voltage (approx 0.7 volts). A conventional reference electrode, ground pad or bone screw is connected through a current meter to the power supply and acquisition system ground terminal. This biases the recorded signals around 0 V.

The absolute maximum input range for the device is determined by the gate to source breakdown voltage, likely at least +/− 20 V. Further protection from transients, such as those caused by cardiac defibrillation can be added with standard electrostatic discharge (ESD) protection techniques.

The device is expected to remain fully operational when exposed to gamma radiation during fluoroscopic procedures because the level of radiation exposure is orders of magnitude lower than levels known to cause performance changes in silicon transistor circuits of this size (19). However, further testing is needed to fully qualify the performance of this device while exposed to radiation.

Circuit Fabrication

The fabrication starts with the preparation of the polyimide substrate (25 μm) (Kapton). For ease of handling, a sheet of this material was attached to a glass slide coated with a thin layer of poly(dimethylsiloxane) as a soft adhesive. Separately doped silicon nanoribbons were prepared through a high temperature diffusion process using a p-type silicon-on-insulator (SOI) wafer (Si(260 nm)/SiO_2(1000 nm)/Si) (SOITEC) and phosphorous spin-on-dopant (SOD) (P509) (Filmtronics). A 300-nm thick layer of SiO_2 deposited by plasma enhanced chemical vapor deposition (PECVD) served as the diffusion barrier mask. Doping regions were defined through conventional photolithography and CF_4/O_2 reactive ion etching (RIE). The diffusion was performed at 950~1000 C in a rapid thermal annealing (RTA) system. A series of wet etching steps with HF and piranha solution (H_2O_2 and H_2SO_4 mixture) removed the SOD and SiO_2.

Doped nanomembranes derived by patterned etching of the top silicon layer of the SOI wafer were transfer-printed onto the polyimide substrate with a thin, spin cast layer of a precursor to polyimide as an adhesive. To prepare the structures for transfer, the buried SiO_2 layer was etched away with concentrated HF solution to yield freestanding nanomembranes. The polyimide precursor was cured at 300 C for 1 h immediately after printing. Further isolation of the active Si components, such as source, drain and channel regions, was accomplished by photolithography and reactive ion etching with SF_6. A thin gate oxide of SiO_2 (~100 nm) was then deposited by PECVD. The source/drain contact regions were opened with buffered oxide etchant through a photolithographically patterned mask. The gate electrodes and metal interconnects were deposited by electron evaporation of Cr/Au (~5 nm/~145 nm) and patterned through wet etching. Each unit cell contains seven transistors,

interconnected by wiring as described in the main text. Isolation of the metal layers was accomplished with a polyimide interlayer dielectric with thickness of 1.4 μm. Connections between layers were established through holes defined by patterned reactive ion etching with O_2. A stack of organic/inorganic insulation layers followed by encapsulation with a photocurable epoxy (SU8) (Microchem Corp) formed a water-tight seal. After insulation, we used the flexible heat seal connector to connect the electrodes with the data acquisition system through an adapter circuit board. The design of this adapter board is shown in Fig. S17. Detailed insulation and heat seal connection processes are described in following sections.

Barriers to Biological Fluids

Because the measurement environment is wet and contains a large number of ions from the saline solution, a multilayer barrier strategy is used to prevent leakage currents that would be dangerous for the animal. An inorganic/organic multilayer and an additional thick organic insulation layer were used for this purpose (Fig. S3 and S4). After spin coating the PI interlayer dielectric and subsequent dry etching to create vias, the first metal layers are connected to the second metal layer (yellow) through the first via (purple), which completes the device fabrication process (Fig. S4). In the encapsulation design, we used a staggered via structure, between via 2 and via 3. By intentional misalignment of the vias, the first via can be completely covered by the final epoxy layer. Figure S5 shows the final microscope image after the insulation.

Interconnection Scheme

After device fabrication, the flexible sensor is interconnected to the circuit board through a flexible ACF film. For this connection, heat and pressure are applied. After alignment between ACF film and the sample, clipping with conventional metal clips provides enough pressure for the connection. To prevent mechanical failure in samples during clipping and to spread pressure over the whole connection area, a piece of PDMS and glass can be added (Fig. S6A). After clipping, heating at 180°C for 15min results in a mechanically and electrically sound connection between the metal and ACF film (Fig. S6B, C).

Acquisition System

The adapter circuit board was connected via a standard 40 pin ribbon cable to the main interface circuit board (Fig. S18 – S21). This custom circuit board provided the row select signals to the electrode array and provided buffering of the analog output signals from the array. The buffering was accomplished by TLC2274 op-amps (Texas Instruments). This stage of buffering further reduced the output impedance to allow for longer cable runs and improved switching speed. The outputs of this circuit board were connected to National Instruments PXI-6281 and USB-6259 high-speed M Series multifunction data acquisition (DAQ) modules via standard BNC cables. The DAQ modules were used to generate the row select signals and to sample the multiplexed analog output signals from the electrode array. In total, 18 analog input channels were used. Data were acquired, demultiplexed, stored, and displayed using custom MATLAB software (The MathWorks™, Natick, MA).

Circuit Simulation

Simulations were performed with the spectreS simulator (Cadence) (Figs. S22, S23). The NCSU_TechLib_ami06 tech library was used for all of the transistors.

Data Processing

Data from all channels were high pass filtered at 1 Hz and up-sampled by a factor of 20 to a sampling rate of 12.5 kHz before processing. Up-sampling allowed the relative activation

times to be computed with sub-sample time accuracy since data from multiple heart beats were averaged. After up-sampling, the data were smoothed and demeaned to remove the DC bias. An average signal was constructed, and the derivative was taken to identify the relative activation times by using an automatic peak search algorithm.

Circuit Mechanics

For a thin film of length L and bending stiffness B wrapping on a cylinder of radius R (Fig. S9A), the total energy of the wrapped state is composed of two parts, the bending energy in the thin film U_b and the adhesion energy U_a between the thin film and the cylinder. The bending energy in the thin film is

$$\frac{1}{2}U_b=\frac{1}{2}B\kappa^2L=\frac{B}{2R^2}L. \tag{S1}$$

The adhesion energy is

$$\frac{1}{2}U_a=-\gamma L, \tag{S2}$$

where γ is the adhesion energy (per unit area) between the thin film and the cylinder. If $U_b + U_a < 0$ (the unwrapped state has energy of 0), the wrapped state is energetically favorable, and thus the thin film wraps around the cylinder. This gives

$$\gamma>\frac{B}{2R^2}. \tag{S3}$$

The cross sectional layout of the circuit, which will be used to determine the bending stiffness B, is shown in Fig. S9B. The top SU8 layer has a thickness $h_1 = 18\ \mu m$, Young's modulus $E_{SU8} = 5.6\ GPa$ and Poisson's ratio $\psi_{SU8} = \mathbf{0.22}$ (20). The bottom PI layer has a thickness $h_2 = 25\ \mu m$, Young's modulus $E_{PI} = 3.4\ GPa$ and Poisson's ratio $\psi_{PI} = \mathbf{0.34}$ (21). The middle layer, of thickness ~5, is composed of several different components. The material and thickness of each component is shown in Fig. S9B, and their Young's moduli are: $E_{Si} = 150\ GPa$, $E_{SiO_2} = 72\ GPa$, $E_{Au} = 78\ GPa$, $E_{Si_4N_3} = 194\ GPa$. Since each of these components only occupies a small portion of each layer of material, the position of the mechanical neutral axis can be approximately obtained as (within a few percent error)

$$y_0=\frac{1}{2}\frac{\bar{E}_{PI}h_2^2+\bar{E}_{SU8}h_1\,(2h_2+h_1)}{\bar{E}_{PI}h_2+\bar{E}_{SU8}h_1}, \tag{S4}$$

where $\bar{E}_{PI}=E_{PI}/\left(1-\nu_{PI}^2\right)$ and $\bar{E}_{SU8}=E_{SU8}/\left(1-\nu_{SU8}^2\right)$ are the plain strain moduli of PI and SU8, respectively. The bending stiffness of the circuit is

$$B=\bar{E}_{PI}h_2\left(\frac{1}{3}h_2^2-h_2y_0+y_0^2\right)+\bar{E}_{SU8}h_1\left[\frac{1}{2}h_1^2+h_1\,(h_2-y_0)+(h_2-y_0)^2\right]. \tag{S5}$$

The strain at a point of coordinate y is given by

$$\varepsilon = \frac{y - y_0}{R_b}, \tag{S6}$$

where R_b is the bending radius of curvature of the circuit. The position of the mechanical neutral axis is calculated as $y_0 = 26.5\ \mu m$. With the bending stiffness given by Eq. (S5), Eq. (S3) gives $\gamma > 8.7\ mJ / m^2$. For a bending radius R_b =5 cm, the maximum strain in the Si is and SiO_2 is ~0.001% and ~0.0001%, respectively; the strains in the four Au layers are ~0.001%, 0.004%, 0.03% and 0.05%, respectively.

Animal Experiments

The array was placed on the heart of an adult pig and conformed to the epicardial surface, including epicardial coronary vessels (Fig. 3). Initially, the array was positioned between the epicardium and parietal pericardium, where it was demonstrated to slide easily across the surface of the heart. Subsequently, the parietal pericardium was removed, and the array was left to stay in position via surface tension alone. However, we do not anticipate this to cause a problem during an actual minimally-invasive procedure because there would be additional anchoring force provided by the catheter inducer for the electrode array and the surrounding tissues.

The heart was externally paced via a standard, non-steerable decapolar electrode EP catheter (Boston Scientific, San Jose, CA) held in contact with the epicardial surface.

Supplementary Material

Refer to Web version on PubMed Central for supplementary material.

Acknowledgments

We thank T. Banks and J.A.N.T. Soares for help using facilities at the Frederick Seitz Materials Research Laboratory.

Funding: This work was supported by a National Security Science and Engineering Faculty Fellowship and the U.S. Department of Energy, Division of Materials Sciences under Award No. DEFG02-91ER45439, through the Frederick Seitz MRL and Center for Microanalysis of Materials at the University of Illinois at Urbana-Champaign. Work at the University of Pennsylvania is supported by the National Institutes of Health Grants (NINDS RO1-NS041811-04, R01 NS 48598-04), and the Klingenstein Foundation.

REFERENCES AND NOTES

1. Gelinck GH, Huitema HEA, Veenendaal E, Cantatore E, Schrijnemakers L, Putten JBPH, Geuns TCT, Beenhakkers M, Giesbers JB, Huisman B-H, Meijer EJ, Benito EM, Touwslager FJ, Marsman AW, Rens BJE, Leeuw DM. Flexible active-matrix displays and shift registers based on solution-processed organic transistors. Nat. Mater 2004;3:106–110. [PubMed: 14743215]
2. Cantatore E, Geuns TCT, Gelinck GH, Veenendaal E, Gruijthuijsen AFA, Schrijnemakers L, Drews S, Leeuw DM. A 13.56-MHz RFID system based on organic transponders. IEEE J. Solid-St. Circ 2007;42:84–92.
3. Baca AJ, Ahn J-H, Sun Y, Meitl MA, Menard E, Kim H-S, Choi WM, Kim D-H, Huang Y, Rogers JA. Semiconductor wires and ribbons for high-performance flexible electronics. Angew. Chem. Int. Ed 2008;47:5524–5542.
4. Khang DY, Jiang H, Huang Y, Rogers JA. A stretchable form of single-crystal silicon for high-performance electronics on rubber substrates. Science 2006;311:208–212. [PubMed: 16357225]

5. Kim D-H, Ahn J-H, Choi WM, Kim H-S, Kim T-H, Song J, Huang YY, Liu Z, Lu C, Rogers JA. Stretchable and foldable silicon integrated circuits. Science 2008;320:507–511. [PubMed: 18369106]
6. Sekitani T, Noguchi Y, Hata K, Fukushima T, Aida T, Someya T. A rubberlike stretchable active matrix using elastic conductors. Science 2008;321:1468–1472. [PubMed: 18687922]
7. Kim D-H, Rogers JA. Stretchable electronics: materials strategies and devices. Adv. Mater 2008;20:4887–4892.
8. Ko HC, Stoykovich MP, Song J, Malyarchuk V, Choi WM, Yu C-J, Geddes J III, Xiao J, Wang S, Huang YY, Rogers JA. A hemispherical electronic eye camera based on compressible silicon optoelectronics. Nature 2008;454:748–753. [PubMed: 18685704]
9. Kim D-H, Song J, Choi WM, Kim H-S, Kim R-H, Liu Z, Huange YY, Hwang K-C, Zhang Y-W, Rogers JA. Materials and noncoplanar mesh designs for integrated circuits with linear elastic responses to extreme mechanical deformations. Proc. Nat. Acad. Sci. USA 2008;105:18675–18680. [PubMed: 19015528]
10. Patolsky F, Timko BP, Yu G, Fang Y, Greytak AB, Zheng G, Lieber CM. Detection, stimulation, and inhibition of neuronal signals with high-density nanowire transistor arrays. Science 2006;313:1100–1104. [PubMed: 16931757]
11. Timko BP, Karni TC, Yu G, Qing Q, Tian B, Lieber CM. Electrical recording from hearts with flexible nanowire device arrays. Nano Lett 2009;9:914–918. [PubMed: 19170614]
12. Aliot EM, Stevenson WG, Garrote JMA, Calkins CH, Bella PD, Jaïs P, Kautzner J, Kuck K-H, Lerman BB, Reddy V, Schilling R. EHRA/HRS expert consensus on catheter ablation of ventricular arrhythmias. Europace 2009;11:771–817. [PubMed: 19443434]
13. Scherlag BJ, Lau SH, Helfant RH, Berkowitz WD, Stein E, Damato AN. Catheter technique for recording his bundle activity in man. Circulation 1969;39:13–18. [PubMed: 5782803]
14. Chaudhury MK, Whitesides GM. Direct measurement of interfacial interactions between semispherical lenses and flat sheets of poly(dimethylsiloxane) and their chemical derivatives. Langmuir 1991;7:1013–1025.
15. Qian J, Gao H. Scaling effects of wet adhesion in biological attachment systems. Acta Biomaterialia 2006;2:51–58. [PubMed: 16701858]
16. Michalske TA, Fuller ER. Closure and repropagation of healed cracks in silicate glass. J. Am. Ceram. Soc 1985;68:586–590.
17. Kadish A, Shinnar M, Moore EN, Levine JH, Balke CW, Spear JF. Interaction of fiber orientation and direction of impulse propagation with anatomic barriers in anisotropic canine myocardium. Circulation 1988;78:1478–1494. [PubMed: 3191601]
18. Clerc L. Directional differences of impulse spread in trabecular muscle from mammalian heart. J. Physiol 1976;255:335–346. [PubMed: 1255523]
19. Medhurst PL, Foster DJ. Effects of gamma radiation on threshold voltages of trench isolated CMOS. Electronics Letters 1989;25:1155–1156.
20. Al-Halhouli AT, Kampen I, Krah T, Buttgenbach S. Nanoindentation testing of SU-8 photoresist mechanical properties. Microelectronic Engineering 2008;85:942–944.
21. Yu DYW, Spaepen F. The yield strength of thin copper films on Kapton. J. Appl. Phys 2004;95:2991–2997.
22. TLC2274 Quad Low-Noise Rail-To-Rail Operational Amplifier. Texas Instruments Incorporated; DALLAS, TEXAS 75265: http://focus.ti.com/docs/prod/folders/print/tlc2274.html
23. 3M Round Conductor Flat Cable. .050” 28 AWG Stranded, PVC, http://multimedia.3m.com/mws/mediawebserver?66666UuZjcFSLXTt4Xf6NXF6EVuQE cuZgVs6EVs6E666666--
24. Harrison, R. paper presented at the IEEE 2007 Custom Integrated Circuits Conference (CICC); San Jose, CA. 16 to 21 September 2007;

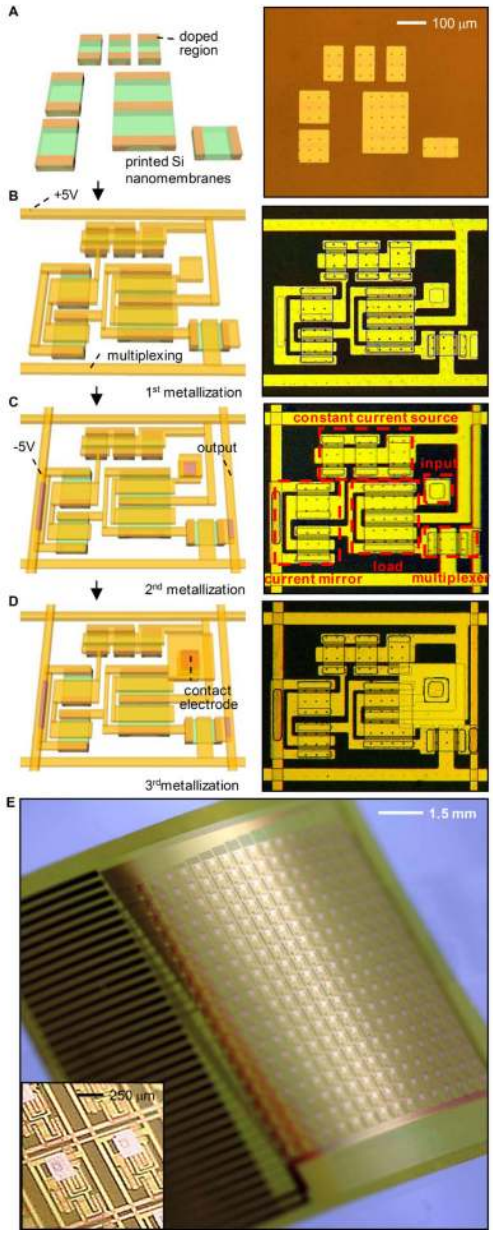

Fig. 1.

Schematic illustration and images corresponding to steps for fabricating active, conformal electronics for cardiac electrophysiology mapping, and photograph of a completed device. **(A)** Schematic illustration (left) and optical micrograph (right) of a collection of doped silicon nanomembranes in a unit cell. **(B)** Configuration after fabrication of the source, drain and gate contacts, with suitable interconnects and row electrodes for multiplexed addressing. **(C)** Configuration after fabrication of the second metal layer, including the column output electrodes. Annotations in the image on the right indicate the multiplexing transistor and the various components of the amplifier. **(D)** Final layout after deposition of encapsulation layers and fabrication of the contact electrode that provides the interface to the cardiac tissue. **(E)** Photograph of a completed device, in a slightly bent state. (Inset) A magnified view of a pair of unit cells.

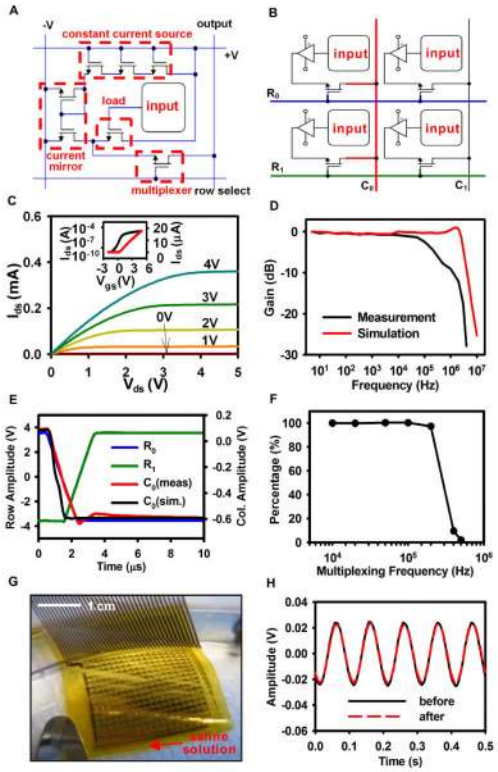

Fig. 2.

Design and electrical properties of an active, flexible device for cardiac electrophysiological mapping. **(A)** Circuit diagram for a unit cell, with annotations corresponding to those in Fig. 1C. **(B)** Circuit diagram of four unit cells, indicating the scheme for multiplexed addressing. **(C)** Current-voltage characteristics of a representative flexible silicon transistor. Drain to source current (I_{ds}) is plotted as a function of drain to source voltages (V_{ds}). The gate to source voltage (V_{gs}) is varied from 0 to 4V in 1V steps. (Inset) I_{ds} on logarithmic (left) and linear scales (right) as Vgs is swept from −2 to +5V, demonstrating the threshold voltage (V_t) of the transistor. **(D)** Simulated and measured frequency response of a representative amplifier with multiplexing disabled. The amplifier shows performance properties consistent with design targets and simulations, i.e. −3 db cutoff frequency of ~ 200 kHz. Simulations were obtained using commercial software (Cadence, Cadence Design Systems; see SM for simulation details). **(E)** Representative multiplexer switching response, showing the row select signals, column output and simulated column output. The response time is limited by the external row select signal slew rate. **(F)** Percentage of the final voltage value attained during the allotted settling time, averaged across all of the electrodes, for increasing multiplexing frequency, indicating that the maximum useable multiplexing rate is approximately 200 kHz. **(G)** Photograph of a completed device with ACF interconnect, immersed in a saline solution. **(H)** Sine wave response (at 10 Hz) before and after saline immersion for 3 hours.

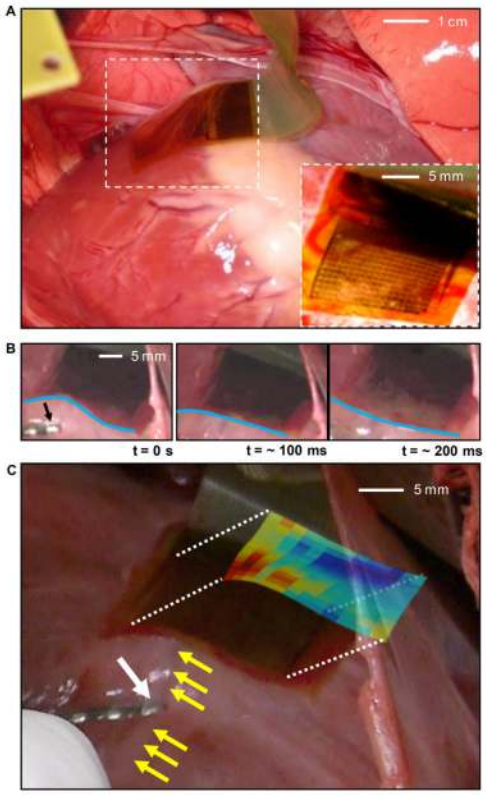

Fig. 3.

Photographs of a flexible EP mapping device in use in a porcine animal model. **(A)** Photograph of flexible device conforming to the cardiac tissue via surface tension. (Inset) A magnified image at a different viewing angle. **(B)** Sequence of movie frames collected at different times during the contraction cycle of the heart, illustrating the ability of the device to bend in a way that maintains intimate, conformal contact with the tissue during cardiac rhythm. Blue lines highlight the degree of bending along the device. A conventional pacing electrode is indicated in the left frame (black arrow). **(C)** Photograph of a device on the left anterior descending (LAD) coronary artery (yellow arrow), with overlaid color map of the relative time of depolarization from paced activation. The white arrow in the lower left indicates the pacing electrode and the red colors in the activation map indicate the areas of earliest response.

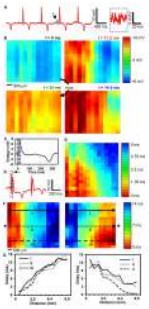

Fig. 4.

Representative data recorded from a porcine animal model with a flexible EP mapping device. **(A)** Representative single voltage trace without external pacing. (Inset) Magnified view of the system noise. Black arrow, source of the inset data. The SNR of the recorded signal was approximately 34 dB. **(B)** Representative voltage data for all electrodes at four points in time showing normal cardiac wavefront propagation. Voltage is plotted with the color scale in the right corner. **(C)** Average voltage from all electrodes illustrating the point in time that each frame in (B) was taken (dotted-line). The color of the dashed lines corresponds to the color of the time label in (B). **(D)** Representative single voltage trace with external pacing from a standard clinical electrode. The black arrow and dotted-line box highlight the pacing artifact. Note that negative is plotted up by convention in A,C, and D. **(E)** Color map of relative activation times for two different external pacing sites. The activation times are plotted with the color scale shown at the right. Asterisks (*) indicate the relative location of the external pacing electrode. The scale bar illustrates the spacing between electrode locations. The data from the activation map at the locations marked by lines i – iii are plotted in (F). **(F)** Activation delay plotted as a function of distance from the left side of the array for selected rows indicated by the arrows in (E). Data from 5 columns in B and 6 columns in E were removed due to failures in the metal interconnections.